Fire Safety Journal 138 (2023) 103795

Contents lists available at ScienceDirect

Fire Safety Journal

journal homepage: www.elsevier.com/locate/firesaf

Simulation of the December 2021 Marshall fire with a hybrid stochastic Lagrangian-cellular automata model

Georgios Efstathiou [a], Savvas Gkantonas [a,*], Andrea Giusti [b], Epaminondas Mastorakos [a], C. Michael Foale [c], Rhonda R. Foale [c]

[a] Department of Engineering, University of Cambridge, Cambridge, UK
[b] Department of Mechanical Engineering, Imperial College London, London, UK
[c] Creede, CO, USA

ARTICLE INFO

Keywords:
Fire propagation
Cellular automata
Random walk
Wildland-urban interface
Marshall fire
Colorado

ABSTRACT

A stochastic model based on a combination of the cellular automata approach for forest fires and a random walk for firebrands and hot gases has been further developed and used to simulate the Marshall fire, Colorado, December 2021. Typical heat release profiles for burning wooden houses from the literature were used to distill information on the burning duration and ignition delay time needed to model the hours-long firebrand emission from wooden buildings in the Marshall area during this fire. In addition to information on vegetation and housing structures from in-person inspection, satellite images were used to estimate various model parameters. The results give reasonable predictions for the extent of the fire and its time evolution. A parametric analysis further highlighted the sensitivity of predictions to the parameters used in the model and suggested areas for improvement. The very low computational cost of the model, ease of operation, and acceptable accuracy suggest that the proposed framework can be used for operational decision-making and damage assessment.

1. Introduction

Devastating wildfires are causing massive destruction to the environment. The combination of a wildfire outbreak near an urban area and the appearance of extreme weather conditions (high wind speeds and draught) leave little time to operate and protect the wildland-urban interface (WUI), resulting in loss of properties and lives. Therefore, there is an increasing need for fast and accurate models that can process real-time weather data and geographical information to predict the evolution of such complex phenomena and support decision-making when attempting to control deadly wildfires. In addition, pre-evaluating fire scenarios before the development of any fire can help firefighters and authorities to manage different emergency scenarios. This paper further develops a novel stochastic modelling approach for a WUI fire evolution using fine-grained local information on land and building flammability that serves the above purposes.

Most of the WUI fire modelling attempts in the literature usually deploy empirical or semi-empirical mathematical relations, probabilistic models, and data-informed models [1–7] to simulate fire propagation. However, these models generally rely on a statistical or phenomenological description of the observed fire behaviour and require a large amount of hard-to-find data from historical fires [8]. Other approaches coupling computational fluid dynamics and mechanistic combustion models can also be considered (e.g., see Ref. [9]), but their computational cost can be prohibitive for real-time predictions in large-scale fires.

Typically, models suitable for real-time operational use aim to estimate the fire's rate of spread (ROS) and the fire perimeter in homogeneous terrains, thus lacking the ability to describe the smaller-scale characteristics and the patchy behaviour that is often observed in a WUI fire. Fire propagation in the WUI is the most challenging to predict due to differences in fire behaviour between a forest and an urban area, which need to be integrated and combined in a single model. In particular, capturing fire transmission at the interface between the forest and the residential buildings requires knowledge of the ignition and thermal properties of the materials involved, as well as a model capable of capturing the intrinsic stochasticity of the fire propagation process. In addition, it would be of great value to be able to predict the probability that the fire will reach a particular point, information that could guide fire prevention and risk management through the design and planning of land plots.

The recent focus on the cellular automata approach in fire propagation modelling is promising and has resulted in the development of new models [10–18], thus offering real-time support for fire suppression and

* Corresponding author.
E-mail address: sg834@cam.ac.uk (S. Gkantonas).

https://doi.org/10.1016/j.firesaf.2023.103795
Received 8 August 2022; Received in revised form 12 March 2023; Accepted 10 April 2023
Available online 15 April 2023

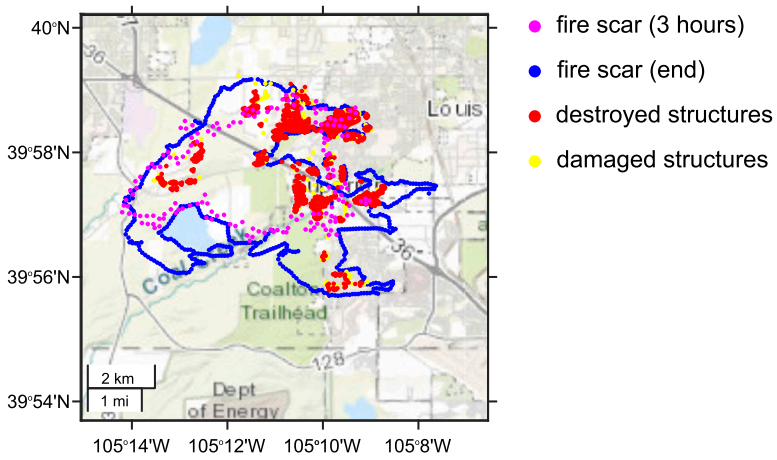

Fig. 1. Regional map showing the outline of the final burnt region (fire scar) from satellite data (blue), the fire scar 3 h after ignition (magenta), the damaged structures (yellow), and destroyed (red) structures during the Marshall fire. This map is a digitised version of the map presented in Ref. [20]. The fire scar 3 h after ignition is based on Ref. [21]. (For interpretation of the references to colour in this figure legend, the reader is referred to the web version of this article.)

evacuation actions. However, their use in WUI fires has not yet been extensively studied or demonstrated. These models incorporate physical information in their grid cells and account for the inhomogeneous properties that are inherently present at the WUI. The appropriate set of rules and processes that determine the fire transmission between cells is the key component and main challenge to the successful prediction of WUI fires when using cellular automata models. The limits of cellular automata models are mainly related to a lack of neat distinction between the flammable material and the propagation modes, which implies the necessity of empirical/semi-empirical relations to make the model predictive. To overcome this drawback, Mastorakos et al. [19] have proposed a new approach, called *FireSPIN*, that combines the cellular automata approach with stochastic virtual fire particles. As in the cellular automata approach, the terrain is modelled as an ensemble of cells with different properties. However, the information on fire propagation is advanced through the tracking of Lagrangian fire particles representing the wildfire transmission phenomena such as convection, firebrands, and radiation. This conceptual separation between the terrain (emitter and receiver of the fire information) and the propagation of information offers a flexible framework for physics-based modelling of fire dynamics.

In this paper, we further develop the previously proposed stochastic Lagrangian-cellular automata model *FireSPIN* [19] by introducing a more detailed description of the flammable material, especially making a distinction between flora and buildings. This is incorporated via the use of different ignition delay times and total burning duration for each cell (e.g., pixel in a terrain map) in the inhomogeneous terrain examined. We demonstrate the model's potential to capture all the features of a WUI fire by simulating the case of the Marshall fire in Colorado, 2021, which, according to satellite data and eyewitnesses, showed a very intermittent behaviour with strong variations in propagation speed, thus making it a challenging test case. Our work aims to develop a predictive tool with real-time capabilities that will combine the exploitation of detailed geographical information, weather predictions, and a consistent description of the physics involved.

The rest of the paper is structured as follows. First, the prevailing conditions and specifics of the Marshall fire are discussed based on media information, satellite data, and a field investigation. Next, the methodology used in the simulations is presented with a particular focus on cell flammability and modelling choices. This is followed by the simulation results, discussion, and a sensitivity analysis in which selected parameters and features of the model are investigated. Key conclusions close the paper.

2. Marshall fire overview

The following information is based on media outlet information and some own field investigations post-fire. On December 30th of 2021, a wildfire broke out near Highway 93 in Boulder County, Colorado, around 11 am. High-speed winds combined with a long drought period caused the fire to spread quickly and reach nearby towns (Superior, Louisville, and Broomfield) in a matter of minutes. The fire continued to burn until heavy snow fell on the night of 31st December–1st January. The aftermath was 1084 destroyed and 149 damaged residences that expanded across the three towns, as shown in Fig. 1. According to official reports [22] and Refs. [23,24], the final total burnt area was 6026 acres. Other sources (e.g., see Ref. [24]) reported the burnt area at 6200 acres during an advanced fire stage, but we will consider the officially reported value as the ground truth for our comparisons. One person was killed, and one person is still missing [24].

According to the National Weather Service (NWS) [25] and Ref. [26], high winds developed in the morning hours before the fire, as a result of a mountain wave travelling over the Front Range Mountains and Foothills. This phenomenon generated very high wind speeds, strong gusts and extreme turbulent events moving down the mountain slope and onto the plain, thus fanning the fire constantly during the day with very persistent westerly winds travelling at 50–60 mph (≈22.5–27 m/s) and gusting up to 100 mph near the vicinity of Marshall Lake. The described phenomenon is reflected in the gust speeds reported by NWS. Near the eastern towns, the winds decelerated but still gusting up to 68 mph (Superior, 2 pm). Finally, after a few hours, the intense winds stopped, which resulted in slower fire propagation.

The fire was initially developed on homogeneous grasslands far from the towns of Superior, Louisville, and Broomfield. This type of vegetation, characterised by short ignition delay times, was responsible for the rapid fire spreading during the first minutes. In the three towns of interest, the neighbourhoods usually comprised wooden buildings and tall vegetation, favouring long-lasting fire sustenance, while in some residential areas, there are concrete buildings that act as deterrents to further fire spread. According to witnesses [27,28], the fire was characterised by thick high-speed smoke and firebrands. Together with radiation, these are the primary mechanisms for fire propagation and are included in the model.

3. Methods

3.1. Modelling framework

The basics of the *FireSPIN* (Fire Stochastic Particle Integrator) model have been previously presented in Ref. [19], but the key features are

repeated here for clarity. In addition, some variations are discussed to take into account the difference in flammability of the region with uniform low vegetation *vs.* the built area, including the type of building (wooden or brick). In summary, fire propagation is modelled by considering the state of the discretised land (the "cells") and the evolution of virtual "fire particles" emitted from these cells to mimic the mechanism by which one cell can transmit the fire to a close or distant neighbour. The trajectory and state of these particles aim to mimic the turbulent dispersion of gases and/or firebrands and their cooling off due to air entrainment. What happens when one of these particles visits a new cell depends on the cell's flammability and contents, which are modelled through an ignition delay time (e.g., infinite for non-flammable regions, small for quick-to-ignite vegetation, and intermediate for cells that contain wooden houses) and the expected burn duration. Further details on the above concepts are given in the following, including a description of the modifications over the original framework in Ref. [19].

3.1.1. The cells

The area of interest is discretised in cells (square-shaped in this implementation, but can be of any shape) based on the resolution available in the satellite data. Information on the flammability of each cell is obtained by examining these data, as discussed in Section 3.2. Each cell contains its own particles. These are activated and begin to move one by one once their "mother" cell is visited by a burning particle from another cell (close or remote). The emission rate of the particles can be thought of as equivalent to the heat release rate (HRR) of the flammable material enclosed in the cell of interest. One or many particles may be released at once and at a suitable time, approximating the HRR profile as an instantaneous process, or their release may be spread over time to better represent the HRR profile. The latter mechanism can be parameterised by using an ignition delay time (τ_{ign}), marking the time difference between the arrival of a burning particle from another cell and the release of a new particle (as in the peak of the HRR profile), and the total burning duration (τ_{burn}), marking the total duration of self-sustaining burning. The selection of these parameters is explained later, but at this point, note that the current implementation is different from Ref. [19] where the true ignition delay time and burn time are incorporated into a single timescale (single particle release).

3.1.2. Virtual particles and random walk

The model uses two types of particles. The first one, called "convective particles", is used to model the convection of gases and firebrands and their turbulent dispersion under the assumption of a random walk motion. The governing equations can be written in a 2-D representation as follows:

$$\frac{\mathrm{d}Y_{\mathrm{st,p}}}{\mathrm{d}t} = -\frac{Y_{\mathrm{st,p}}}{\tau_{\mathrm{mem}}}; \tag{1}$$

$$\mathrm{d}X_{i,p} = F_l\, U_{i,p}\, \mathrm{d}t, \text{ where } \; i = 1,2; \tag{2}$$

$$\mathrm{d}U_{i,p} = -\frac{(2+3C_0)}{4}\frac{u'}{L_t}(U_{i,p} - U_{w,i})\,\mathrm{d}t + (C_0\,\varepsilon\,\mathrm{d}t)^{1/2}\mathcal{N}_i. \tag{3}$$

The random walk of Eq. (3) is based on the well-known Lagrangian description of turbulent dispersion [29], supplemented with a simple decay of the scalar $Y_{\mathrm{st,p}}$ (Eq. (1)) following the Lagrangian PDF method for reacting flows [29]. $Y_{\mathrm{st,p}}$ denotes the "burning state" of a particle, as will be explained later. u' and L_t are the turbulent velocity fluctuations and the integral length scale, respectively. Their combination gives an estimate of the dissipation rate of turbulent kinetic energy $\varepsilon = (u')^3/L_t$ [30]. C_0 is a constant close to 2, and $\mathcal{N}_{\mathrm{i}}$ is a random variable normally distributed with zero mean and unit variance. $U_{\mathrm{w,i}}$ is the component of the wind speed in the ith direction and $U_{\mathrm{i,p}}$ is the current velocity component of the particle, which is scaled by a factor F_l when updating the new particle position in Eq. (2) to account for the fact that a fire usually propagates at a speed that is slower than the wind speed ($F_l \sim 0.1$) [31].

Note that in the current implementation, we do not separate gaseous motion from firebrand motion, but their composite effect is lumped together. It is very straightforward in a future implementation to separate these two mechanisms, that is, to use the above equations with a given random walk, F_l, and τ_{mem} for gases and a separate random walk and τ_{mem} for firebrands, thus allowing very fine-grained information on the emitting fire and propagation mechanism to be built into the framework. Furthermore, fire-induced modifications of turbulence [32,33] and refined firebrand trajectories and evolution [34,35] can easily be included.

Once a particle is emitted, it is considered to have a burning state that is maintained as long as the corresponding scalar quantity $Y_{\mathrm{st,p}}$, remains above a certain limit (Y_{lim}). $Y_{\mathrm{st,p}}$ takes values from 0 to 1 and, while $Y_{\mathrm{st,p}} > Y_{\mathrm{lim}}$, the particle travels according to the random walk motion and ignites the cells that intersect its trajectory. The decay of $Y_{\mathrm{st,p}}$ is exponential and is dictated by τ_{mem}. Eq. (1) can also be viewed as equivalent to Newton's law of cooling so that $Y_{\mathrm{st,p}}$ stands for a normalised temperature difference, indicating whether the particle is hot ($Y_{\mathrm{st,p}} > Y_{\mathrm{lim}}$), that is, capable of igniting another cell, or cold ($Y_{\mathrm{st,p}} < Y_{\mathrm{lim}}$), and therefore not capable of igniting further fire. The initial burning state (normalised temperature difference), Y_{init}, assigned to each particle could also be used to simulate the magnitude of the HRR profile, thus complementing the function of τ_{ign} and τ_{burn} in characterising the flammability and energy release of a cell. However, here we assume $Y_{\mathrm{init}} = 1$ in the initial state, and we discuss the effect of this assumption separately using simplified model problems in Appendix A.

The second type of particles can be used to model fire propagation under no-wind conditions and the effect of radiation. These particles move according to the following equations:

$$\mathrm{d}r_p = \overline{S_{f,0}}\mathrm{d}t + \sigma_{S_{f,0}}(\mathrm{d}t)^{1/2}\mathcal{N}_r; \tag{4}$$

$$\mathrm{d}\theta_p = 2\pi\mathcal{N}_\theta. \tag{5}$$

In Eqs. (4)–(5), r_p and θ_p define a radial coordinate system with an origin in the centre of the mother cell of the particle (indicated in the following with the subscript 'mc'), so that the coordinates of the particle can be given at any time as $X_{1,p} = X_{1,\mathrm{mc}} + r_p\,\cos(\theta_p)$ and $X_{2,p} = X_{2,\mathrm{mc}} + r_p\,\sin(\theta_p)$. $\mathcal{N}_r$ and $\mathcal{N}_\theta$ are random variables normally distributed with zero mean and unit variance. $S_{f,0}$ is the no-wind propagation speed, which in Eq. (4) is assumed to follow a normal distribution with mean $\overline{S_{f,0}}$ and standard deviation $\sigma_{S_{f,0}}$. In Ref. [19], $S_{f,0}$ was considered constant, i.e., $\sigma_{S_{f,0}} = 0$, and equal to 0.1 m/s for one type fuel, but it could generally be a function of space and local conditions. The $Y_{\mathrm{st,p}}$ of the "radiation particle" follows Eq. (1) but with a decay timescale $\tau_{\mathrm{mem}} = L_r/S_{f,0}$, where L_r is a characteristic radiation length (e.g., in the order of O(100) m). Note that the radiation model is here added mainly for completeness and it is not used, unless stated otherwise. Since the fire examined was wind-driven, the effect of radiation-driven propagation is expected to be small.

The implementation of the governing equations involves the choice of a suitable particle computational timestep, Δt, and maximum grid size, Δx_{max}, for the area of interest. For example, to adequately resolve particle decay, the timestep should be much smaller than the particle lifetime, which by integration of Eq. (1) requires $\Delta t \ll -\ln(Y_{\mathrm{lim}}/Y_{\mathrm{init}})\,\tau_{\mathrm{mem}}$. To ensure accuracy and stability for the tracking of the first type of particles, the timestep should also be smaller than the integral time scale of turbulence and should also correspond to a particle Courant number, c, below unity [36]. These criteria may be written as in $\Delta t = c \cdot \min(\Delta x/|U_p|, L_t/u')$, where Δx is the actual grid size used (assuming square cells). As discussed in Ref. [37], Δx_{max} could represent the distance eddies carry a particle during a timestep. According to Eqs. (2)–(3), a particle generated in the centre of a cell has a higher

Table 1
Original classes from the NLCD database [38] and cell flammability parameters used in the simulations.

Original classes	Final class	Ignition delay time (s)	Total burning duration (s)
Developed areas with concrete buildings (–)	7	∞	0
Developed high-intensity areas (24)	6	1500	15 000
Developed, medium-intensity areas (23)	5	1000	9000
Developed low-intensity areas (22)	4	180	360
Open water, perennial ice/snow (11,12)	3	∞	0
Developed open space, barren land (21,31)	2	∞	0
Vegetation and rest of the classes	1	30	180

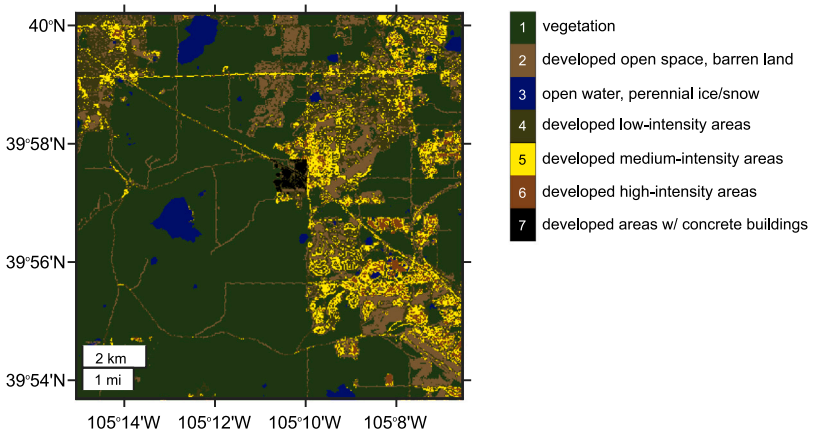

Fig. 2. Visual representation of the computational domain. The different colours display the area of interest as interpreted by the NLCD database [38]. (For interpretation of the references to colour in this figure legend, the reader is referred to the web version of this article.)

probability of travelling a distance smaller than $F_l(C_0\epsilon\Delta t)^{1/2}\Delta t$ during a timestep Δt. Therefore, the neighbouring cell centre should be at a distance not larger than two times that distance to resolve propagation accurately. Substituting for $\Delta t = L_t/u'$, the upper limit of the grid spacing becomes proportional to the integral length scale, as in $\Delta x_{\max} = 2F_l C_0^{1/2} L_t$. As in Ref. [19], the particles are released from the centre of the cell. The sensitivity of the predicted fire spread to the grid size and the number of virtual particles used per cell, N_p, will be shown later.

3.2. Fuel map and cell flammability parameters

The area of interest was discretised on the basis of the information provided by the *NLCD 2016: USGS National Land Cover Database, 2016 release* (NLCD) [38]. In this database, 20 different bands dictate the classification of cells in a 30 × 30 m^2 spatial resolution. For the sake of simplicity (complementary to the lack of sufficient literature sources), the bands were here grouped into seven Classes as shown in Table 1 and Fig. 2. The main differences between the Classes can be identified in terms of the modelling parameters concerned with the flammable material's burning behaviour: τ_{ign} (time difference between the cell's first particle emission from the first landing of a fire particle from a neighbour) and τ_{burn} (duration of the cell's burning, which is equal to the time difference between the first and last particle emission from this cell).

The cells classified as Class 1 are mainly populated by grasslands that experienced a remarkably long drought period in the months before the Marshall fire broke out, and as a result, they are expected to ignite and burn fast. Based on Refs. [39,40], the flame residence time (as defined by Anderson [41]) for grass fuel could be in the range of 7–44 s, therefore it would be reasonable to assume that τ_{ign} is of the same order. In the absence of detailed HRR profile data, an appropriate choice for τ_{burn} is more challenging, but we may presume that the shape of the HRR profile follows the burning of experimentally studied cellulosic fuels, as in Ref. [42], and that τ_{burn} is O(10) times larger than τ_{ign}. Our estimates are provided in Table 1, although these could be revisited in the future.

Classes 2 (see brown coloured cells in Fig. 2), 3 (blue), and 7 (black) are assumed to be indestructible and hence have infinite ignition delay time and no burning duration. Furthermore, these cells do not emit any particles, even if visited by a burning one. The cells in Class 7 were manually selected after observing Google Earth images and our in-person inspection images. The choice of this Class is also justified by the fire scar depicted in Fig. 1, where it is clearly shown that buildings prevented the fire from propagating downwind in some regions. Regarding Classes 4, 5 and 6, the choice of their parameters is rather challenging due to the diversity of the construction materials used in the buildings. In this case, it can be seen that the most common Class inside the towns of interest is 5 (yellow). A typical neighbourhood in Louisville consists of several houses, small roads, and tall trees. This layout is similar to the one studied by Himoto et al. [43], where a block of model two-storey wooden houses, separated by small roads and covering about 300 m^2, resulted in a burning duration of approximately 3000 s. Himoto et al. [43] also reported HRR profiles of individual houses, as well as the accumulative HRR of the block. These profiles have three distinct phases: (i) a growth phase, (ii) a fully developed phase, and (iii) a decay phase. To provide an appropriate rationale for the selection of timescales that correspond to the burning process, τ_{ign} and τ_{burn} were chosen based on the times that correspond to the start of the developed phase and the end of the decay phase, respectively.

It should be noted that the HRR profiles of the individual houses, compared to the accumulative HRR, highlight a dependence of the timescales on the burning area due to the fire propagation from house to house. The three phases for a single house last considerably less than the same phase for the entire block. As a result, considering larger cell sizes compared to the block of houses studied in Ref. [43] requires the assumption of longer (in time) HRR profiles. Of course, the dependence of the HRR profile on cell size is not exclusive; therefore, other factors could drastically alter the shape and width of the HRR (e.g., the type of construction materials or the humidity history). Here, we approximate the timescales associated with similar blocks of houses in a coarser resolution (30 × 30 m^2) by extrapolating and observing how these vary from a "house scale" (3.6 × 3.6 m^2) to a "block scale" (17.4 × 16 m^2)

in Ref. [43]. In future work, this extrapolation could be generalised or even completely avoided by using satellite data of much finer resolution so that houses, gardens, trees, and roads could be better distinguished.

In Ref. [43], the duration of the three phases in the individual HRR profiles varied from 200–800 s with a typical duration of 500–600 s, while for the entire block, this time was 3000 s, hence a linear scaling between cell size and its burning duration is not prohibitive. In our case, this yields a burning duration of about 5200 s; however, a higher value of $\tau_{\text{burn}} = 9000$ s seemed more appropriate to also account for the more prominent presence of concrete materials and open spaces. As far as τ_{ign} is concerned, the fully developed phase in Ref. [43] started at about 450 s for a single house, whereas the corresponding time could reach 600 s for the whole block (first peak in the accumulative HRR). Consequently, extrapolating linearly τ_{ign} with cell size might not be appropriate, but a value of O(1000) s is reasonable considering also the presence of concrete materials and wider open spaces.

Classes 4 and 6 may be better viewed as a "mixture" of Classes 1 and 5. A Class 4 (dark yellow) cell is mostly covered by vegetation (tall trees and grass) and open spaces. Therefore, it is expected to ignite and burn faster compared to built areas (180 s and 360 s), but not faster compared to a grassland cell due to the sparsity of vegetation and the different plants that normally exist in urban areas (tall trees and low clean cut vegetation). Finally, Class 6 cells are highly developed areas, where non-flammable surfaces account for 80% to 100% of the total cover and the buildings are mostly apartment complexes, rows of houses, and commercial/industrial structures. For this Class, we assume a larger ignition delay time and burning duration due to the absence of vegetation and wooden buildings. Table 1 summarises our choices of τ_{ign} and τ_{burn} for all Classes, and their effect will be further analysed in Section 5.3.

3.3. Modelling parameters

In addition to τ_{ign} and τ_{burn}, the model requires the definition and calibration of several other parameters as summarised in Table 2. A calibration against controlled fire experiments has already been performed in Ref. [19]. A sensitivity analysis can offer a comprehensive insight into the effect of the rest (this is done in Section 5) but some of the parameters can be rationally chosen between reasonable limits.

For example, the integral length scale of turbulence, L_t, is based on turbulent boundary layer theory (e.g., see Ref. [44]) and was chosen as the height of the fire, but also as a representative gust size, i.e., O(10–100) m. The normalised turbulence intensity, A (typically in the range 0.2–0.4), is characteristic of the turbulence levels inside the atmospheric boundary layer (e.g., see Ref. [45]) divided by the local mean velocity (not the free-stream one). Note that empirical formulas for A and L_t usually consider natural winds and not extreme weather events (large gusts), such as those encountered during the Marshall fire. Consequently, turbulence length scale and intensity estimates should be towards the upper end of typical ranges and higher.

Finally, the number of new particles emitted and their phasing is a key input to the model. For simplicity, we assume that $N_p > 1$ particles are released uniformly throughout the burn duration. The same number is assigned to each cell regardless of the cell flammability (see Table 1), even though the primary intention is to use more than one particles (e.g., $N_p = 20$) to better emulate prolonged emissions of hot gases and firebrands from housing structures.

3.4. Simulation setup

The area of interest is a 12×12 km^2 square, as shown in Fig. 2. It was discretised in a 400×400 grid, resulting in a resolution similar to the information provided by the NLCD, that is, each cell is a 30×30 m^2 square, which proved fine enough to satisfy all the grid spacing criteria discussed in Section 3.1. The model needs wind speed and direction as input. Two different zones were defined to account for the prevailing wind conditions present in the domain, as explained in Section 2. During the first hours of simulation, west of Superior, the wind was set to be West (270 deg) 25 m/s (≈55 mph), while east from Superior, the wind was reduced to half this value (based on a comparison between the data from Refs. [26,46,47] for Marshall Lake and the town of Louisville). After 4 h, the wind speed gradually decreased, following the trends reported in Ref. [46]. Note that in future applications of the model, the wind speed and direction, as well as the local level of turbulence, may originate from real-time measurements or numerical weather prediction models, further improving the characterisation of the wind.

It is also known that the fire started near the intersection of Highways CO-93 and CO-170, close to Eldorado Springs. It was reported that at some point the fire was burning on both sides of CO-93; therefore, five cells west of the intersection point were used as ignition points. To evaluate the temporal evolution of the fire and the initial fire spread while also getting a good representation of the final total burnt area, the first 14 h of the event were simulated and statistics were gathered over many code realisations. Finally, a 23-h simulation of the Marshall fire was attempted, mainly to observe the fire propagation of a well-established fire in the WUI under lower wind speeds.

Table 2
Main modelling parameters and the corresponding values used in the baseline simulation.

Name	Symbol	Baseline value
Velocity factor of particles	F_l	0.15 [19]
Memory timescale (s)	τ_{mem}	10 [19]
Burning state threshold	Y_{lim}	0.2 [19]
Initial burning state	Y_{init}	1 [19]
Turbulence length scale (m)	L_t	80
Turbulence intensity	A	0.4
Number of particles per cell	N_p	20
Ignition delay time (s)	τ_{ign}	Table 1
Total burning duration (s)	τ_{burn}	Table 1

3.5. Output processing

The algorithm produces various outputs. The most important one is the ignition state of a cell, i.e., the information on whether a particular cell has been ignited or not (in which case it is assumed that it will eventually burn completely since it will release all its fire particles). It should be noted that firefighting actions can be included at any time by limiting the emissions of particles, but such actions were not included here. From each realisation of the model, each cell is declared to have survived or burnt, and this metric then leads to an evaluation of the probability that the fire reaches a cell, P_b. This probability constitutes a key quantitative output of the model. The fine-grained flammability information associated with the Class allocated to every cell allows P_b to be reported at a spatial resolution equal to the cell size. Many realisations are needed to have a statistically meaningful P_b, but the statistical convergence rate also depends on the number of particles allocated to each cell. Unless stated otherwise, the present analysis is based on 400 realisations, although a lower number was also satisfactory for the present problem and modelling choices. In addition, the pathlines and time evolution of the particles are essential qualitative features of the output, as they can help with insightful visualisations of the fire spreading as a function of time, even from individual realisations.

4. Results and discussion

This Section presents the predicted temporal evolution of the fire and results from individual realisations and averages over many realisations. The statistical convergence of the averages is also discussed, as well as the computational performance of the approach.

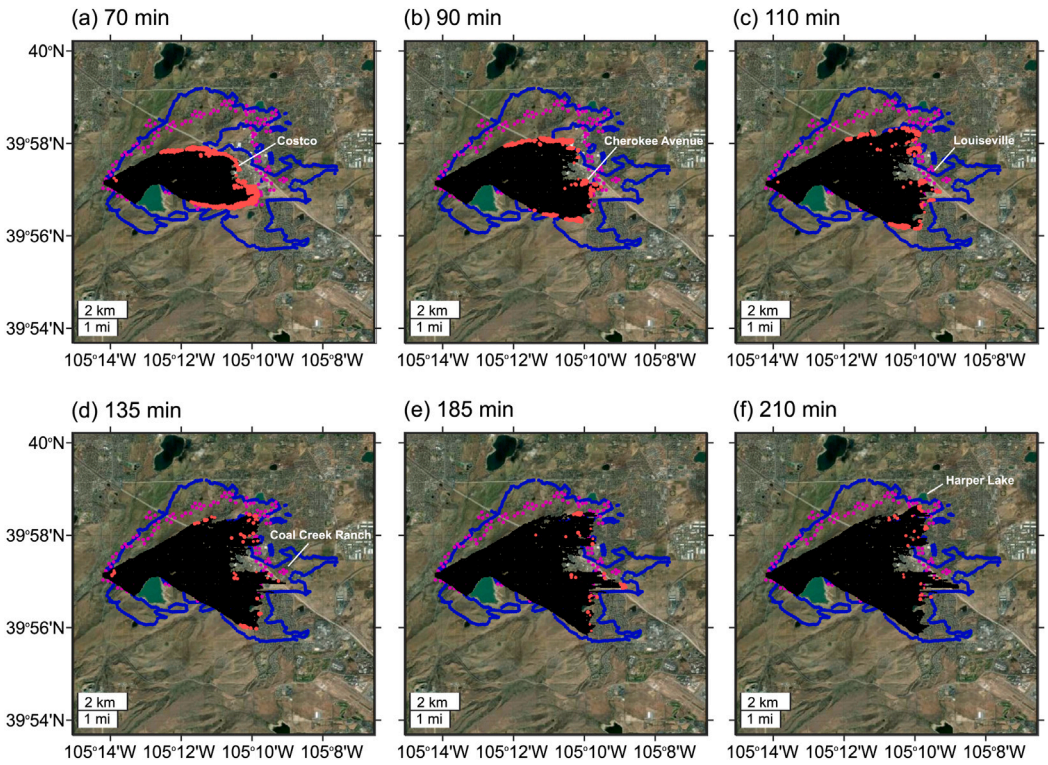

Fig. 3. The evolution of the Marshall fire at the indicated times after ignition. The blue dots show the final fire scar from the satellite data of Ref. [20] and the magenta dots indicate the fire scar 3 h after ignition from Ref. [21]. The red dots represent the currently active convective particles from one realisation. The completely burnt cells that have already emitted all their particles are marked with black. (For interpretation of the references to colour in this figure legend, the reader is referred to the web version of this article.)

4.1. Minute by minute evolution of the fire

Figs. 3 and 4 show the predicted temporal evolution of the fire and satellite observations of the fire scar (blue dots) on top of an aerial photograph depicting the area of interest (see also Fig. 1). In Fig. 3, the evolution of the fire is visualised by the location and state of virtual particles from a single realisation, while in Fig. 4, the results are presented in terms of probability contours of the burnt area, $P_b(x, y)$. According to the timeline in Ref. [28], it is known that the fire started around 11 am, and the first notable events are the evacuation of Costco at 12:10 pm and the reported fires at Cherokee Avenue and Mohawk Circle around the same time (12:15 pm). Shortly after (12:30 pm), 320 Cherokee Avenue was reported to be engulfed in flames, and at 12:40 pm, the firefighters reported that they were outmatched in Superior and left the area. Two snapshots of the simulated fire at $t = 70$ min and $t = 90$ min from initiation (i.e., at 12:10 pm and 12:30 pm) are shown in Figs. 3–4. It is evident that the model reproduced these events. The good agreement is the result of the appropriate choice of τ_{ign} for the grassland areas and the turbulence characteristics (L_t and A) because until that point the fire was mostly a grass fire, developing on a homogeneous terrain.

At 12:50 pm, the fire was reported to have jumped Highway 36, resulting in the Cool Creek Ranch neighbourhood burning at 1:13 pm (Area 3 in Fig. 5). The model did not predict that the fire would jump the road in this region. This is probably due to the lack of highly accurate weather and satellite inputs. Figs. 3–4 show the fire spread at $t = 110$ min and $t = 135$ min (i.e., at 12:50 pm and 13:15 pm). Although the Coal Creek neighbourhood does not appear to be burning, it can be seen that the fire propagated toward this area at a reasonably accurate speed and that it had actually spread to the northern parts of Louisville by that time.

According to Ref. [21], at 2:05 pm, the fire was at its northern point, burning houses close to Harper Lake. This is also confirmed by reports at 2:30 pm that state that the fire was burning houses in the southern area of Harper Lake along McCaslin Boulevard. The simulation results at these two times are shown in Figs. 3e and 4e. Finally, at 3:40 pm, the fire reached its southern parts and could be observed from Highway Colorado 128. At that time, the model displays an active fire front burning houses in that region, but it has to be noted that the snapshots at earlier times display a premature propagation towards Broomfield.

The fire spread at the intermediate stages is well captured, especially in the northern areas, giving an approximate 10% agreement in terms of the total burnt area with observations at 2:05 pm. Note that the simulated fire spread at $t = 185$ min (i.e., at 2:05 pm) is compared with the observed fire spread as reported at that time [21] and not the total burnt area after the end of the fire. More specifically, the observed fire spread covered approximately 16 000 km^2, while the predicted total burnt area (black marked area) is about 14 400 km^2. As discussed earlier, an over-prediction can be spotted at that time to the southern part and the town of Broomfield. In this study, we assume a constant wind direction (270 deg), and this naturally induces uncertainties and may cause the above over-prediction.

4.2. Burn probability distributions

Fig. 5a shows the probability contours of the burnt area (P_b) in the area of interest 14 h after ignition compared to satellite observations of the fire scar (blue dots). The model captures the overall shape of the burnt area well and gives a good estimate of the fire spread. The use of appropriate τ_{ign} and τ_{burn} for each pixel classification resulted in a reasonable agreement between the actual and predicted propagation through residential areas, thus giving a good estimate of the perimeter of the fire. Based on the P_b isolines, it can be concluded that P_b is mostly unity in the core of the observed burnt area and that there is a sharp transition to zero at the boundaries of the fire scar. On closer inspection, it is evident that P_b has sharp gradients at many locations, suggesting that the model captures the patchy behaviour of a WUI fire.

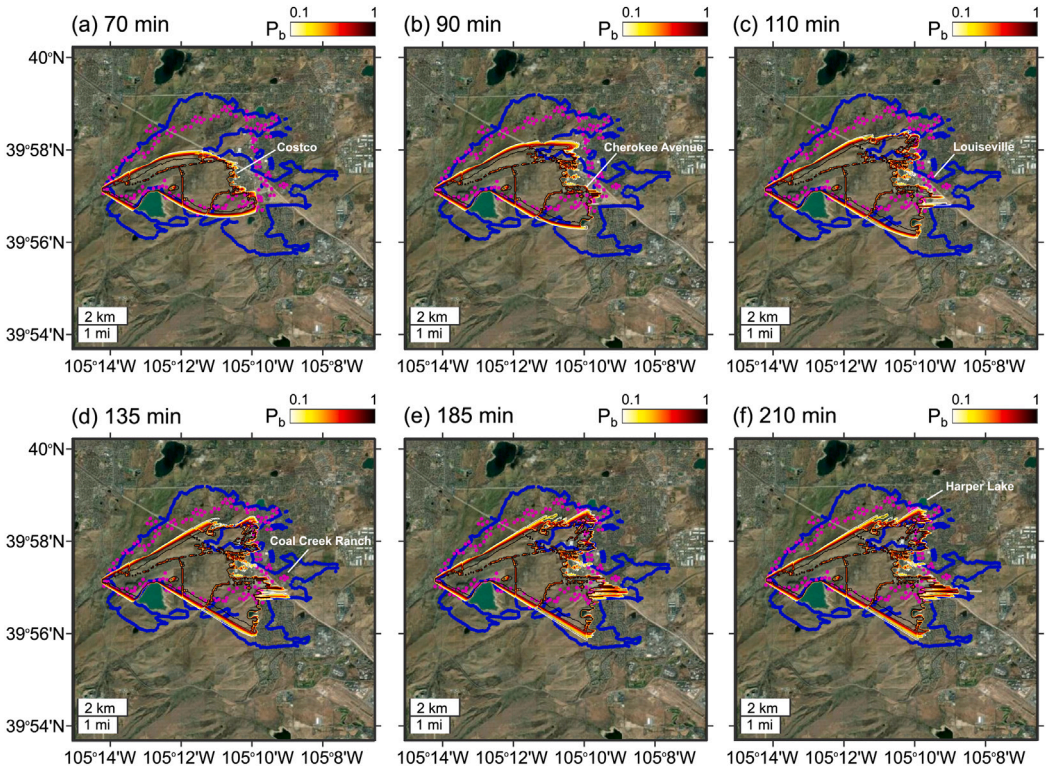

Fig. 4. The evolution of the Marshall fire based on burnt area probability isolines at the indicated times after ignition. The blue dots show the final fire scar from the satellite data of Ref. [20] and the magenta dots indicate the fire scar 3 h after ignition from Ref. [21]. (For interpretation of the references to colour in this figure legend, the reader is referred to the web version of this article.)

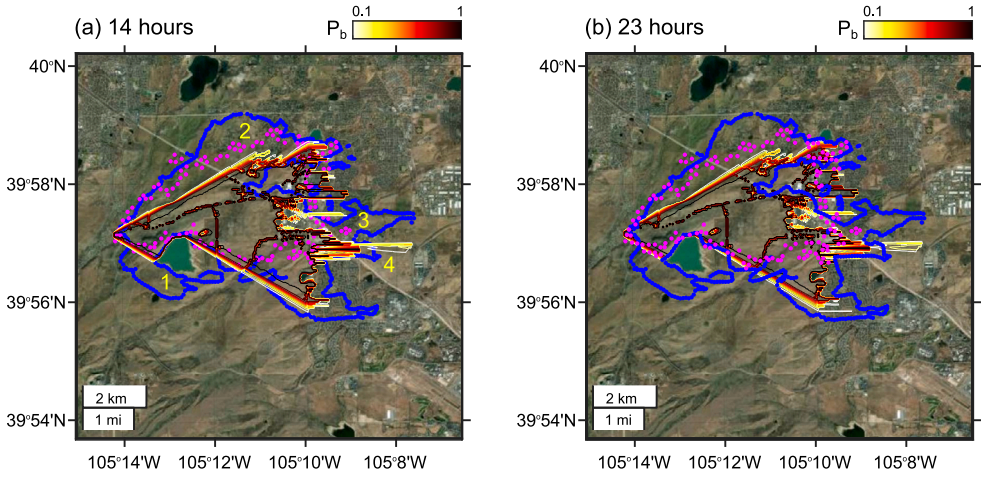

Fig. 5. Burnt area probability isolines at (a) 14 h and (b) 23 h after ignition, based on 400 and 150 realisations, respectively. The blue dots show the final fire scar from the satellite data of Ref. [20] and the magenta dots indicate the fire scar 3 h after ignition from Ref. [21]. The numbers 1, 2, 3 and 4 indicate specific areas of interest discussed in the text. (For interpretation of the references to colour in this figure legend, the reader is referred to the web version of this article.)

From Figs. 3–4 it is evident that the ROS is considerably higher during the initial grass-fire phase compared to the later slow burning in the built area. This important observation demonstrates how the model can adequately capture the transition from a rapidly evolving crown-type wildfire to a slower-burning WUI fire. A patchy behaviour and an unstructured fire front shape are also predicted, consistent with observations. Considering the reported fire extent at 10 pm on December 31st and the final burnt area [24], it is reasonable to assume that most of the important events describing the fire had already taken place by that time. Probably the calmer winds, the sporadic snowfall, and the firefighting actions after that time put the fire under control, thus limiting the fire spread until the heavy snowfall ended the event later that night. To this end, the simulation at $t = 23$ h from ignition (11 pm–10 pm the next day) is shown in Fig. 5b. A full simulation video is also provided in the Supplementary Material. It becomes evident that no significant changes are observed in the total burnt area compared to the simulation until 14 h after ignition. However, it should be noted that dynamical changes in local τ_{ign} and τ_{burn}, corresponding to fire suppression actions and snowfall or rain, were not incorporated into our simulations. The model captured a long hour sustained fire front, slowly

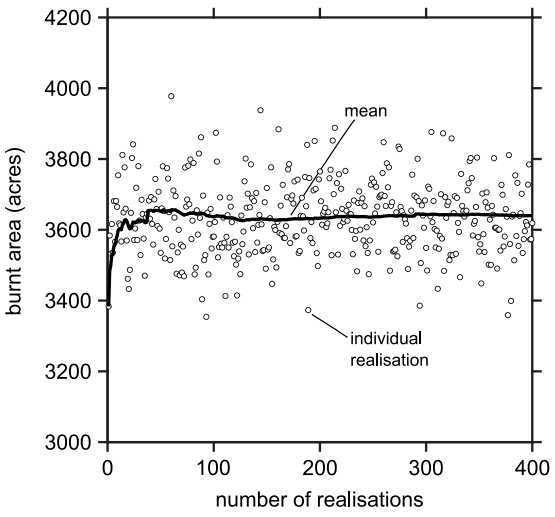

Fig. 6. Predicted burnt area and statistical convergence over 400 realisations.

burning houses in the towns of Louisville and Broomfield, but without dramatically increasing the fire's perimeter. This behaviour is in satisfactory agreement with the observations and shows the model's ability to simulate long-hour-lasting urban fires. Quantitative improvements can be made by fine-tuning the model inputs.

The P_b data shown in Fig. 5a were computed from 400 realisations. The statistical convergence of the model can be assessed from Fig. 6, where the average total burnt area is plotted as a function of the number of realisations. The fire is known to have burnt about 6000 acres, and here we plot the statistics based on the predicted burnt area. Approximately 150 realisations are sufficient to obtain the same results for the first moment of the ignition probability density function. However, it should be noted that the standard deviation is such that a considerably lower number of realisations (here between 20–40) or even a single realisation can be used as an indicative estimate. It is also evident that statistical convergence generally depends on the total amount of particles considered over a single or many realisations; therefore, the number of particles emitted per cell (N_p) and the number of realisations provide complementary routes to access the full sample space of fire front evolution [19]. Nevertheless, it should be reminded that the number of particles released and their phasing is also aimed at approximating (discretising) the HRR of a cell's flammable content, therefore changing N_p (and the release frequency) can affect the statistical convergence rate and fire propagation in a non-linear way, when the initial particle burning state Y_{init} is not suitably adjusted. The effects on fire propagation are further discussed in Section 5, where N_p is varied parametrically. Options for adjusting Y_{init} are also briefly discussed in Appendix A.

Fig. 7 shows zoomed-in images of P_b close to the edge of the fire at $t = 14$ h from ignition. Various interesting features can be observed. First, the bulk of the flammable cells have burnt with very high probability, suggesting that the extensive destruction was not a statistical fluke, also evident from the model convergence shown in Fig. 6. Second, non-flammable cells in the middle of the burnt area can protect cells downwind (e.g., see the green cells that denote flammable but untouched by fire to the right of the white cells). However, in some cases, the turbulent motion and random emission of firebrands emitted by neighbouring regions can also lead to fire spread on the leeward side of non-flammable cells with substantially high probability. The fact that a range of ignition probabilities can be observed in Fig. 7, with P_b being in the intermediate range between 0% and 100% in some areas within the WUI and at the fire scar, is a key strength of the model that has never been demonstrated and underlines how the proposed modelling framework can capture spatially-varying randomness due to local fuel heterogeneity and wind patterns. The only model with some similarities to this work and the possibility of predicting P_b is perhaps the stochastic method by Boychuk et al. [48,49] which is based on a continuous-time Markov chain lattice. Although the aim of that model was to incorporate random spotting mechanisms and showcase differences with deterministic spread models, which cannot provide P_b but only average behaviour, the underlying fire spread processes were not in a physically reasonable form.

The *FireSPIN* model successfully reproduces the patchy behaviour of a typical WUI fire and the prediction of fire characteristics on the neighbourhood scale was demonstrated. There are various aerial photographs [50] showing entire neighbourhoods burnt to the ground, except for one or a few intact houses. It is expected that with the availability of higher resolution geographical information, the model's capabilities can be extended to house-scale fire risk prediction. The model did not capture well the fire propagation in the areas marked 1, 2, 3 and 4 in Fig. 5a. According to satellite observations, the fire spread south of Marshall Lake, thus burning a large area of grass (area 1) that was not captured by our model. However, our in-person inspection and the satellite data suggest that this branch of the fire was not integrated into the fire's main body east of Marshall Lake, and thus did not affect the fire's spread further. This is an important observation, since the model predicted with very good accuracy the southeast branch of the fire that eventually reached the town of Broomfield. Area 2 is also mostly covered with vegetation, with a sparse distribution of houses, but the initial underestimation of the fire-front thickness did not allow for a good capture of the fire's northern part. In area 3, the land is mainly covered with vegetation and the model did not predict the fire crossing Highway 36 in this region, so it could not propagate further. In area 4, where the land is also mainly covered with vegetation, the model predicts propagation with a non-negligible probability ($P_b \approx 20\%$) past the observed fire scar, but fire spread is predicted with greater certainty within the fire scar, as desired.

The discrepancies between the model and the observations in these areas are attributed to the uncertain inputs (e.g., geographical information, weather). In particular, it is likely that under current conditions, the normalised turbulence intensity A may have been higher and not necessarily following a Gaussian distribution: occasional gusts can change direction significantly more than a uniform mean flow plus a cross-stream Gaussian fluctuation, which is what the model uses, might suggest. As previously discussed, wind characterisation can be improved in future studies using more refined measurements or numerical tools (e.g., see [9]). However, some insight into the sensitivity of predictions to various parameters, including A, may already be drawn by performing a series of numerical tests, as will be shown later in Section 5.

4.3. Computational performance

The presented computations were performed on a 2 GHz Quad-Core Intel Core i5 processor. A single full simulation of the baseline case required a $\tau_{\text{CPU}} \approx 1$ h ("CPU time") using a simple model implementation in MATLAB, which is suitable only for proof-of-concept purposes. The same model was also implemented in a serial C++ code where improvements in data transfer between cells and particles demonstrated a $\tau_{\text{CPU}} \approx 4$ min when considering both radiation (e.g., with $L_r = 50$ m) and convective particles and in $\tau_{\text{CPU}} \approx 5$ s when considering only the convective particles.

The computational time per hour of real time varied significantly. The first two hours were by far the most expensive, and this can be attributed to two factors. First, computational time is strongly related to the number of active particles and their interactions with the cells. Since the fire was initially grass-type, the particles were emitted faster than later times (see Fig. 3). Second, during the first hours, the wind speed was significantly higher compared to the last hours of the Marshall fire, which naturally affected the selection of the timestep,

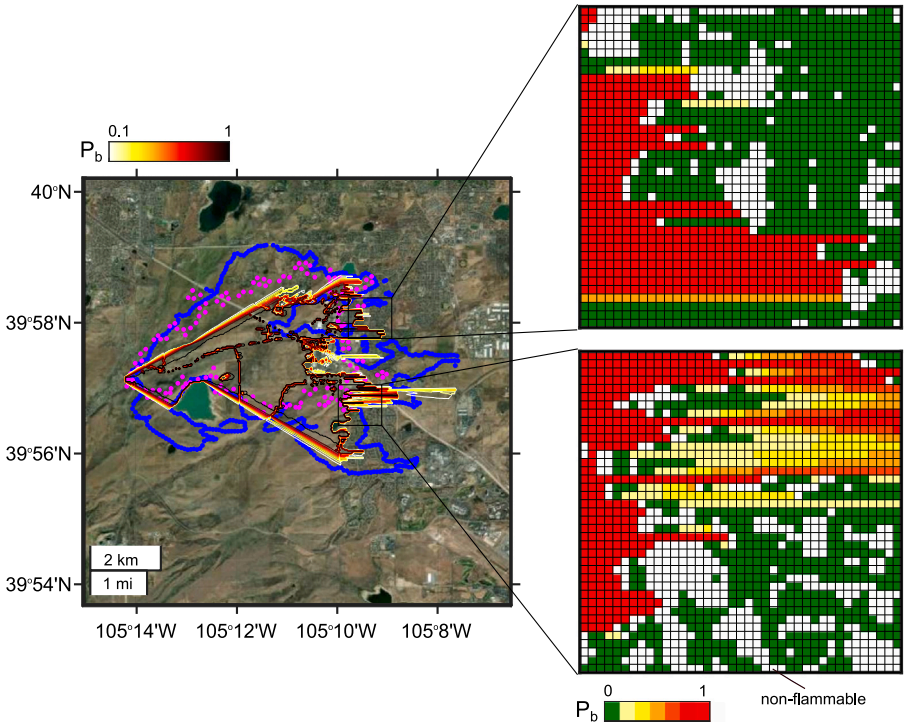

Fig. 7. Zoomed-in image of burnt area probability at 14 h since ignition (see also Fig. 5) for two indicative areas (both 1.2 × 1.2 km^2 wide). Non-flammable cells are indicated with white (see also Classes 2, 3 and 7 in Table 1). Green denotes zero burn probability for flammable cells, and red denotes unity P_b. (For interpretation of the references to colour in this figure legend, the reader is referred to the web version of this article.)

yielding smaller values. Therefore, even if the same number of active particles was present in the domain, the total number of iterations to simulate 1 h would still be higher.

The CPU time is significantly lower than the actual fire evolution (even with the simple MATLAB implementation) and allows for multiple code realisations in a matter of seconds. This performance highlights the real-time capabilities of the model and its possible use for operational decision making.

5. Sensitivity analysis

The sensitivity of the model to the grid characteristics (flammability inputs and resolution) and its main modelling parameters is discussed in the following. The modelling parameters investigated here are N_p, τ_{burn}, τ_{ign}, A and Y_{lim}. Understanding their effect on the model's results is necessary for a better assessment and improvement of their calibration process based on physical information.

5.1. Fuel distribution and grid size

Every fire propagation model is sensitive to flammability inputs. In the following, we examine how the fuel distribution affects the predictions by manipulating the NLCD dataset [38] presented in Section 3.2 as follows. First, we obtain the fuel distribution and flammability information, that is, the ignition delay and the burning duration, at a coarser resolution than the one in the original dataset (Fig. 8a), equal to a cell area of 120 × 120 m^2. This is equivalent to agglomerating groups of 16 cells (pixels) in Fig. 2. Then we split each cell again into 16 subcells to obtain the same resolution of 30 × 30 m^2 as the original dataset (Fig. 8c). This is done to remove effects of grid size on the motion of the virtual particles and only modify the fuel distribution. In the same manner, we modify the NLCD dataset to obtain the fuel distribution at an intermediate resolution of 60 × 60 m^2 (Fig. 8b).

Fig. 9 shows the probability contours of the burnt area in the area of interest 14 h after ignition compared to the satellite observations of the fire scar, similar to Section 4.2. The results show some differences between the three cases, but without specific underestimation or overestimation trends with respect to the large-scale characteristics and overall spread of the fire. In particular, the predicted total burnt area was 3399 acres with a sampling resolution of 60 × 60 m^2 (Fig. 9b) and 3690 acres with a sampling resolution of 120 × 120 m^2 (Fig. 9c), as opposed to the baseline prediction of 3622 acres. Note that these figures are based on cells with non-zero P_b and not only 100% probability of burning. They are also based on 400 realisations, ensuring statistical convergence in all cases and, therefore, suggesting that the fuel distribution primarily affects predictions at the neighbourhood scale and the interface between flammable and non-flammable areas (here toward the east boundary of the fire scar). As expected, different gradients in flammability modify the stochastic behaviour of the fire, whereas the predicted patchiness is reduced when using a coarser sampling resolution, as is evident from the sharp gradients in the probability contours. These characteristics are sufficient to further affect propagation, with the biggest difference here manifested in area 4 (see Fig. 5a), where P_b changes from approximately 20% in the baseline case to almost 100% when the sampling resolution is coarser.

In the baseline implementation, the area of interest has been discretised into square-shaped cells according to the resolution available in the satellite data, providing a cell area of 30 × 30 m^2. In the following, we investigate the sensitivity of predictions to changes in grid size that share the same fuel distribution. However, this sensitivity analysis should not be viewed as a "grid independence" test because, in general, the timescales linked to burning should also be adjusted when working at different resolutions. As discussed in Section 3.2, the adjustment of burning timescales is necessary to capture the correct propagation speed, especially when there are wooden building blocks with hours-long firebrand emission. In addition, for the current model implementation, the use of different cell sizes requires an adjustment of the number of particles to account for the different contents of flammable material within a cell, since virtual particles are used as a means of discretising energy release. In the following, we do not adjust

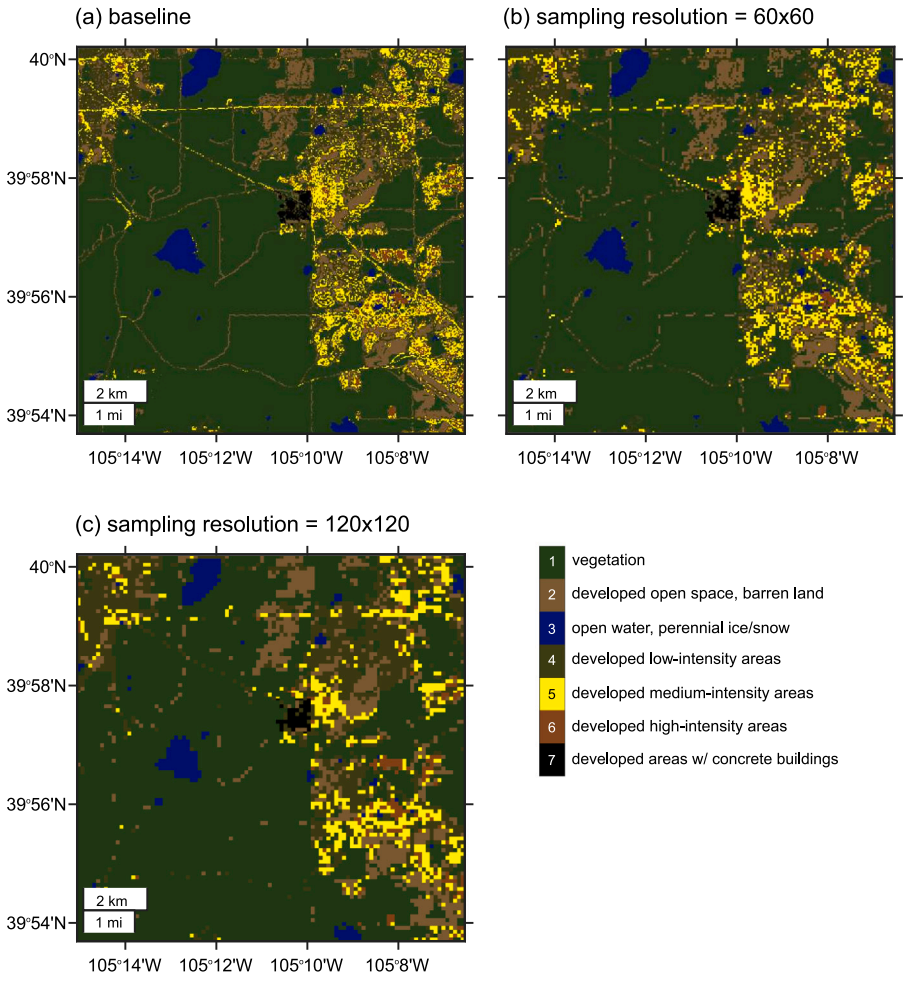

Fig. 8. Visual representation of the computational domain using (a) the baseline fuel distribution and (b-c) a "coarser" fuel distribution using an intermediate sampling resolution of (b) 60 × 60 m^2 and (c) 120 × 120 m^2. All data have the same grid size as in the baseline case. The different colours display the area of interest as interpreted by the NLCD database [38]. (For interpretation of the references to colour in this figure legend, the reader is referred to the web version of this article.)

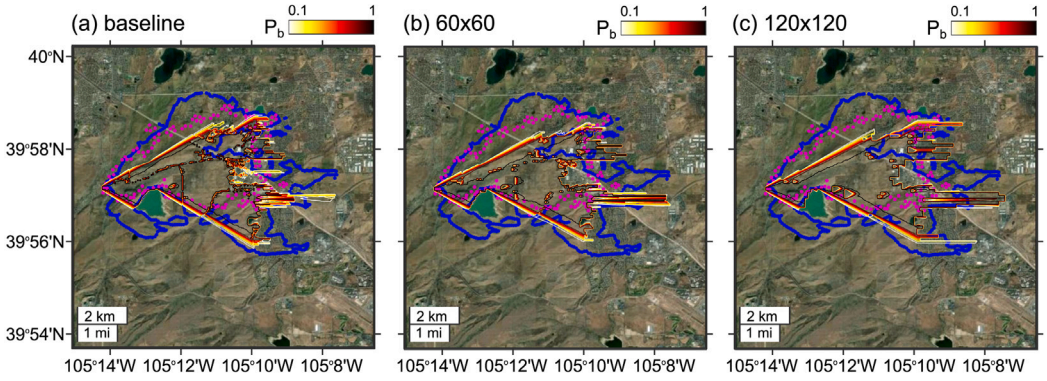

Fig. 9. Sensitivity of burnt area and P_b to the distribution of fuel. The baseline case is shown in (a) 14 h after ignition. A "coarser" fuel distribution is used in (b-c) with an intermediate sampling resolution of (b) 60 × 60 m^2 and (c) 120 × 120 m^2. The blue dots show the final fire scar from the satellite data of Ref. [20] and the magenta dots indicate the fire scar 3 h after ignition from Ref. [21]. (For interpretation of the references to colour in this figure legend, the reader is referred to the web version of this article.)

any burning timescale, but we retain the initial particle density per unit area, ρ_p, similar for all grid sizes, which here range from $\Delta x = 7.5$ m to $\Delta x = 120$ m. In the baseline case, a total of 20 particles per cell were used, which is translated as $\rho_p = 20/900$ particles per m^2. Note that the baseline density would require the use of 1.25 particles per cell in the highest resolution case, which is, of course, not realistic and therefore, we here use two particles per cell for this case (ρ_p is 60% higher).

The analysis is based on the fuel map in Fig. 9c (sampling resolution of 120 × 120 m^2) to avoid mixing of cell fuel properties when switching from higher to lower resolutions. Fig. 10 shows the probability contours of the burnt area 14 h after ignition. First, it is useful to compare the baseline prediction (Fig. 10a) with Fig. 10d, as there is no difference in grid size ($\Delta x = 30$ m) but only in the underlying fuel distribution. Similarly to Section 5.1 and the results of Fig. 9, no major differences are

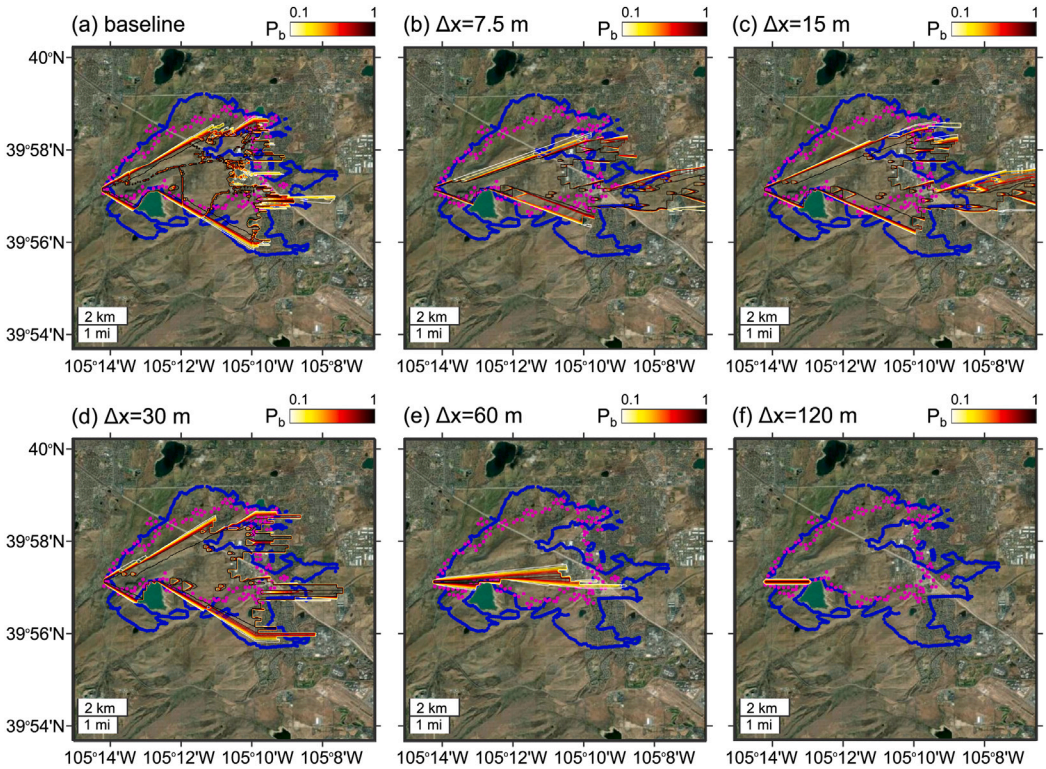

Fig. 10. Sensitivity of burnt area and P_b to the resolution of the grid. The baseline case (having a resolution of 30 × 30 m^2) is shown in (a) 14 h after ignition. The results with the fuel distribution of Fig. 9c and various grid sizes are shown in (b-f). A particle density of 20 particles per 900 m^2 has been used except for (b) where a 60% higher particle density is used. The blue dots show the final fire scar from the satellite data of Ref. [20] and the magenta dots indicate the fire scar 3 h after ignition from Ref. [21]. (For interpretation of the references to colour in this figure legend, the reader is referred to the web version of this article.)

observed with respect to the large-scale characteristics and the general spread of the fire. However, due to the coarser sampling resolution of the fuel map, the predicted patchiness is reduced and the propagation is mostly affected in area 4 (see Fig. 5a) and the southernmost edge of the fire. Second, at resolutions $\Delta x > 30$ m (Fig. 10e and f), it is evident that the movement of the particles is not sufficient to allow probable propagation of the fire, apart from (a few) cells downwind of the ignition point. This is not surprising considering the discussion in Section 3.1, where an upper limit of the grid spacing was proposed. Based on the integral length scale used in this work, the maximum allowable grid size is $\Delta x_{\max} \approx 34$ m and, as a result, a grid size greater than $\Delta x_{\max}$ cannot ensure that a convection particle can be carried far enough to ensure dispersion (and propagation) in all directions. The proposed $\Delta x_{\max}$ grid criterion is therefore numerically justified.

At grid sizes $\Delta x \leq 30$ m (Fig. 10b, c and d), we observe similar behaviour in the fire core but changes in the fire edges that lead to a general decrease in the total burnt area when all cells with either non-zero or only unity P_b are considered. In particular, the predicted total burnt area with $P_b > 0$ is 4032 acres, 3944 acres and 3321 acres with $\Delta x = 30$ m, $\Delta x = 15$ m, and $\Delta x = 7.5$ m, respectively. In addition, we observe substantial changes in the propagation around area 4 (see Fig. 5a) with the fire spreading further toward the east and the north side of the domain with increasingly higher probability when the grid size is reduced. These differences are not attributed to the random walk and the lack of "grid independence" as far as turbulent dispersion is concerned. Instead, as previously discussed, the differences in propagation are mostly affected by the treatment of HRR, which is here approximated with the release of new virtual particles. Even if ρ_p remains similar, the burning timescales τ_{burn} and τ_{ign}, would require calibration with the current model implementation to ensure similar behaviour for various Δx. A sensitivity analysis concerning these timescales is given later in Section 5.3. However, we also argue that the description of a cell's flammable content and its sensitivity to grid size cannot be perfectly ensured unless the particles' initial burning state is also suitably adjusted. This is left for future work, but implementation aspects are also discussed in Appendix A using model problems with uniform fuel distribution.

5.2. Number of virtual particles per cell and Y_{lim}

In addition to the rate of achieving statistical convergence, the number of virtual particles per cell, N_p, also affects the probability of burn. The burnt area probability isolines for the cases of 10, 20 and 30 particles per cell are shown in the top row of Fig. 11. The ratio our baseline ($N_p = 20$) burnt area compared to the cases with $N_p = 10$ and $N_p = 30$ is 0.72 and 1.13, when all areas with $P_b > 0$ are considered. An increasing trend with N_p is therefore evident. As expected, the stochastic movement of the virtual particles increases the predicted fire spread with N_p, but mainly in the lateral direction. The effect of N_p on the fire's extent in the downwind spread and its time evolution is only minor. Note also that the lateral spread is a direct consequence of the magnitude of the cross-wind component of the random walk, which is controlled by the parameter A. A high value of N_p increases the chances of capturing rare events in the sampling over the presumed wind velocity probability density function, and hence the wider fire scar is explained. A more sophisticated determination of A, i.e., including a fire-induced modification of the local gas velocity, or a more rigorous firebrand random walk, can give a different sensitivity to N_p.

Furthermore, it should be noted that the total energy release is perhaps overestimated because all released particles are assigned the same weight in terms of their burning state. For simplicity, the initial particle state Y_{init} was considered here equal to 1, meaning that the total particle lifetime, i.e., when $Y_{\text{st,p}} < Y_{\text{lim}}$ is satisfied, is the same regardless of the burning progress. This situation is equivalent to a relatively constant HRR throughout the burning duration. However,

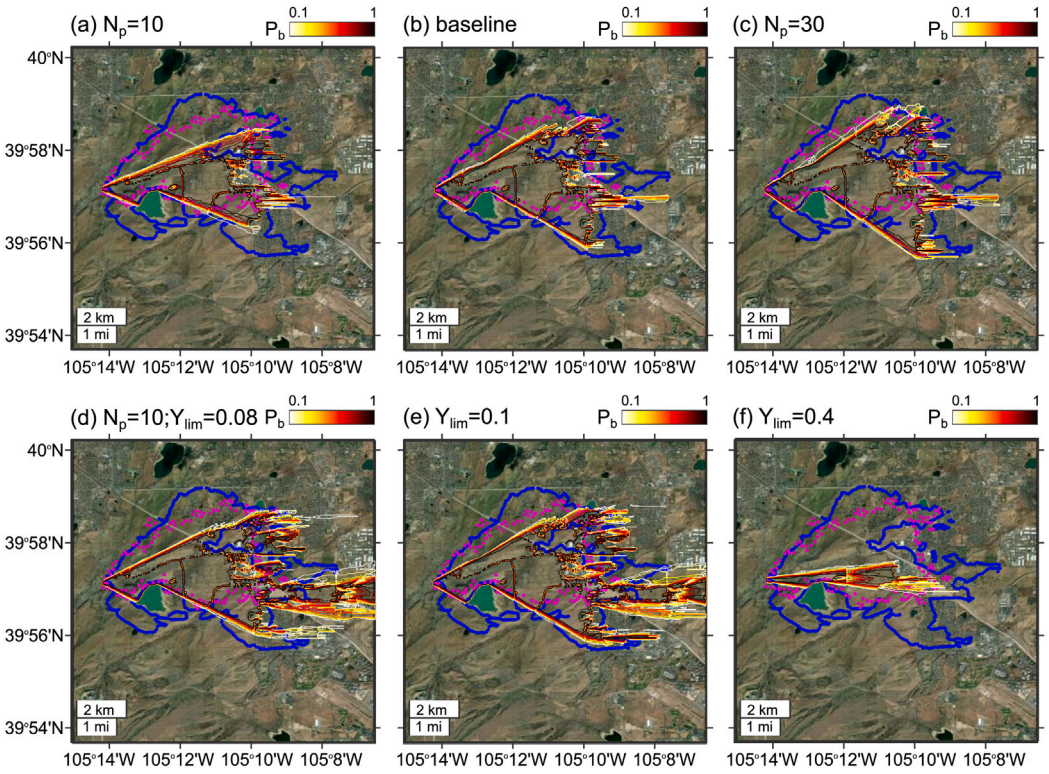

Fig. 11. Sensitivity of burnt area and P_b to N_p and Y_{lim} based on 20 realisations. The baseline case is shown in (b) 14 h after ignition. Results with changes only in N_p are shown above, and results with changes in Y_{lim} (N_p equal to or lower than the baseline of 20 particles per cell) are shown below. The blue dots show the final fire scar from the satellite data of Ref. [20] and the magenta dots indicate the fire scar 3 h after ignition from Ref. [21]. (For interpretation of the references to colour in this figure legend, the reader is referred to the web version of this article.)

this situation may also be unlikely for some construction materials or types of vegetation (e.g., see Ref. [42]); therefore, further research is essential to calibrate all associated parameters against wildfires, experiments or more physics-based approaches, leveraging also available geographical or weather data. Model cases with a different implementation for the initial particle state are presented in Appendix A. In the following, we demonstrate how the burning state threshold, Y_{lim} can affect predictions. The bottom row of Fig. 11 shows the probability of burning for various options of Y_{lim}. Since the particle state is equivalent to a normalised temperature difference, it becomes evident that the longer life span of "hot" particles can enhance fire spread in both the downwind and lateral directions. In particular, major differences are observed west of Louisville, highlighting the importance of this parameter to capture the ROS and ignition probability at the WUI. Smaller values (here $Y_{lim} = 0.1$) allow particles to travel past non-flammable plots of land and reach flammable areas, thus producing a completely different behaviour of the model in several areas, such as area 4 (see Fig. 5a) and the southernmost edge of the fire. Larger values (here $Y_{lim} = 0.4$) reduce the overall fire extent and ROS predicted. Although the selection of Y_{lim} for our numerical tests is rather rigorous (see also Ref. [19]), it can be rationally tuned for other WUI scenarios or computed on the basis of a more detailed energy balance.

5.3. Burning duration, ignition delay and uncertain weather

The correct estimation of τ_{burn} and τ_{ign} is one of the main challenges in connecting the physical characteristics of the cells with the model's input parameters. The different types of vegetation and the various construction materials present in a typical WUI render the selection process very complex; therefore, a more automated process is required. Such a process can be enabled by higher-resolution satellite data that have been classified accordingly to distinguish between materials. Knowledge of the different materials' heat release rate profiles is also required. Complementary to this information, the condition of the vegetation also plays an important role [39,40], and its consideration in the model is equally important, as in fuel models that are already available (e.g., see [51]). Here, we present the effect of a simultaneous ±20% change in the values of τ_{ign} and τ_{burn} used, compared to those in Table 1. Fig. 12 shows the difference in the predicted propagation at $t = 90$ min after ignition. The core of the fire zone is robustly captured, although the edges are slightly different. Similar to what discussed in Ref. [19], the burning timescale affects the ROS (if the timescales are longer, propagation is generally slower) and by extension, the fire front extent, evident here from the angular spread from the ignition point. The behaviour of the model under the uncertainty introduced reveals that τ_{ign} and τ_{burn} are critical in determining both the fire-front thickness and the rate of propagation parallel to the wind speed. This gives prominence to the need for more detailed geographical information on a house scale to allow for a better calibration of such fire propagation models if they are to act as supporting tools for operational decision making.

Fig. 13 shows one case with an extreme choice for the turbulence intensity, that is $A = 1$, to examine the model's behaviour to the weather. Such a turbulence intensity is unrealistic in a turbulent boundary layer, but it is given here as a numerical experiment. Increasing A from 0.4 to 1 results in an expansion of the fire throughout the domain and a clear overestimation of the total burnt area. Therefore, it is obvious that the model is sensitive to the selection of the normalised turbulence intensity. However, the local A selection process can be rationalised if higher resolution weather data are available and more turbulence physics is included. Overall, it is important to highlight the importance of using accurate and comprehensive weather inputs in the model. Nevertheless, the results presented demonstrate that even with simplified information, the model discussed can still produce valuable predictions of reasonable quantitative accuracy when appropriate choices are made.

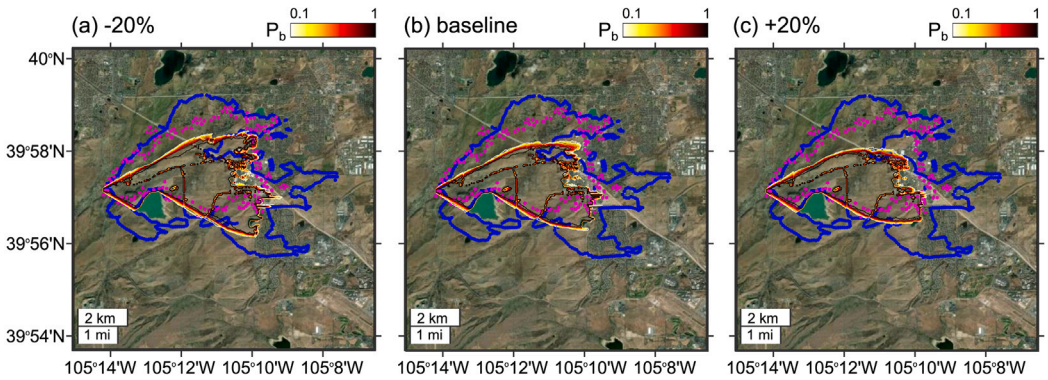

Fig. 12. Sensitivity of burnt area and P_b to τ_{ign} and τ_{burn} based on 20 realisations. The baseline case is shown in (b) 90 min after ignition. Results with a simultaneous ±20% change in τ_{ign} and τ_{burn} are shown in (a) and (c). The blue dots show the final fire scar from the satellite data of Ref. [20] and the magenta dots indicate the fire scar 3 h after ignition from Ref. [21]. (For interpretation of the references to colour in this figure legend, the reader is referred to the web version of this article.)

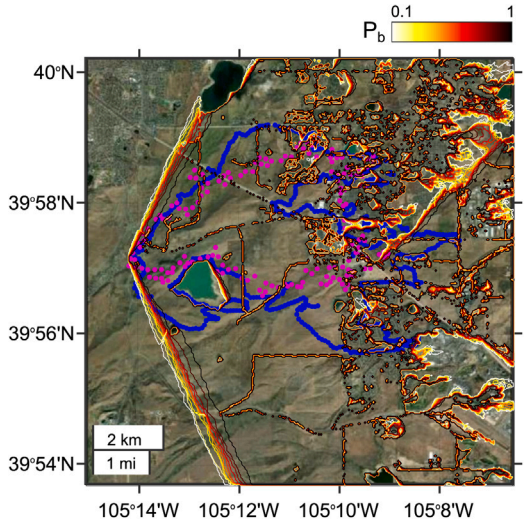

Fig. 13. Burnt area probability isolines at 14 h after ignition with an extreme choice for the normalised turbulence intensity ($A = 1$). The results are based on 20 realisations. The blue dots show the final fire scar from the satellite data of Ref. [20] and the magenta dots indicate the fire scar 3 h after ignition from Ref. [21]. (For interpretation of the references to colour in this figure legend, the reader is referred to the web version of this article.)

Future work requires further validation of the model against historical fires and experiments to better understand and calibrate the modelling parameters (τ_{ign}, τ_{burn}, N_p, Y_{lim}). The initial burning state Y_{init} for each released particle should also be adjusted to better characterise the energy release. Furthermore, a more comprehensive description of slope effects, any fire suppression actions, detailed firebrand temperature history and spatial trajectory, as well as the fire-induced changes in the local wind conditions, need to be incorporated. The present framework allows such developments to be introduced, hence resulting in a comprehensive WUI modelling capability.

6. Conclusions

A previously-developed Lagrangian-cellular automata model was modified to include burning houses and incorporated detailed geographical information. By running it for the December 2021 Marshall fire in Colorado, it was shown that it could predict with reasonable accuracy and efficient computational speed both the large- and small-scale characteristics of a WUI-type fire. The land was discretised into square cells and the NLCD provided each cell's flammability classification in a 30 × 30 m^2 resolution. The model achieved very good agreement with the initial fire propagation until it reached the town of Superior. The accuracy remained satisfactory at both intermediate (t = 3 h since ignition) and later times (t = 23 h since ignition) by producing an approximate agreement of 10% and 30% with satellite observations in terms of the total burnt area. Fine-grained features of the model output include the prediction that areas downwind of the non-flammable regions (or buildings) did not burn and that the probability of burning, P_b, can take intermediate values between 0 and 1, thus allowing the quantification of risk as a function of location and the incorporation of cell-specific flammability characteristics in terms of burn duration and ignition time. The sensitivity of predictions to some of the model's inputs was also studied. The simplicity of the model, its ease of operation, and its minimal computational cost (order of seconds) demonstrate the potential for real-time predictions that can use high-resolution geographic information and weather forecasts.

CRediT authorship contribution statement

Georgios Efstathiou: Methodology, Software, Validation, Formal analysis, Investigation, Data curation, Writing – original draft, Visualization. **Savvas Gkantonas:** Methodology, Software, Validation, Formal analysis, Investigation, Data curation, Writing – review & editing, Supervision, Visualization. **Andrea Giusti:** Methodology, Writing – review & editing, Supervision. **Epaminondas Mastorakos:** Conceptualization, Methodology, Formal analysis, Resources, Writing – review & editing, Supervision, Project administration, Funding acquisition. **C. Michael Foale:** Investigation, Writing – review & editing. **Rhonda R. Foale:** Investigation, Writing – review & editing.

Declaration of competing interest

The authors declare that they have no known competing financial interests or personal relationships that could have appeared to influence the work reported in this paper.

Data availability

Data will be made available on request.

Appendix A. Implementation aspects of the energy release

In the *FireSPIN* modelling framework, the emission rate of new virtual fire particles is equivalent to discretising the energy release from all the flammable content within their "mother" cell and the heat release rate (HRR) profile over time. In addition to the number of particles emitted and their phasing over a prescribed burning duration of a cell, the particle state history, denoted by $Y_{st,p}$, is critical in fire propagation as it controls the ability of particles to ignite close or

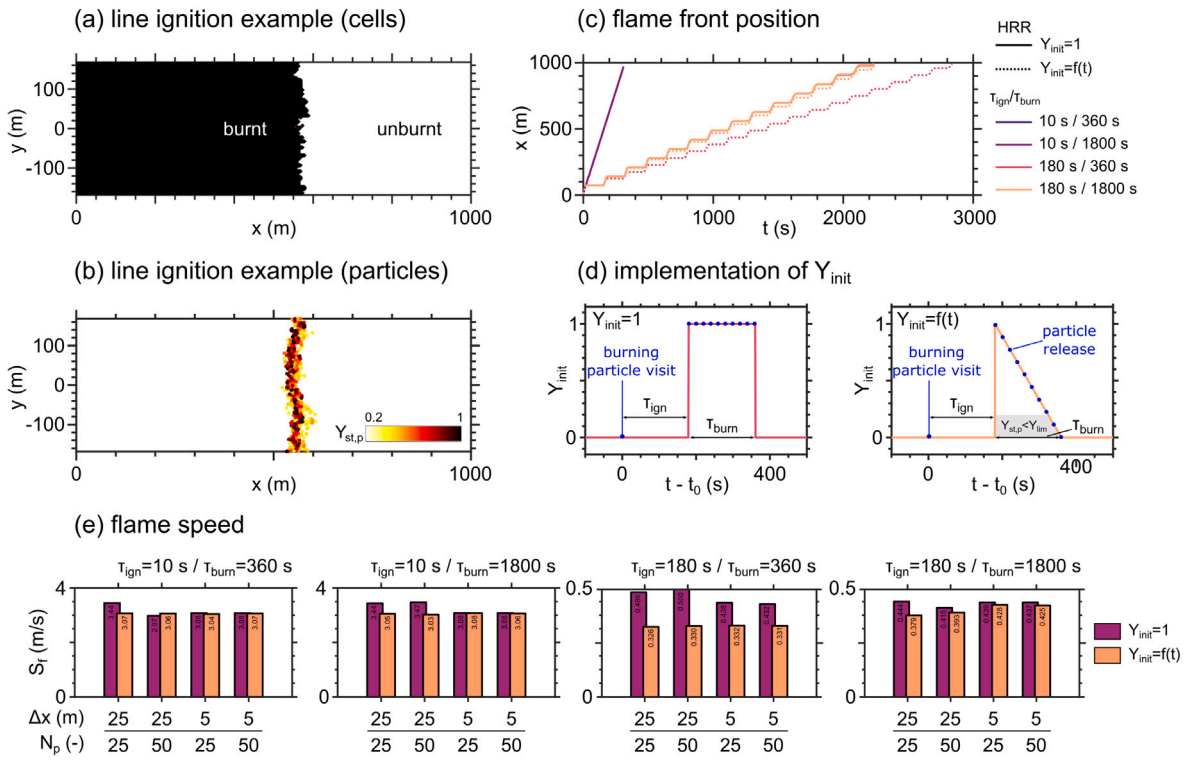

Fig. A.1. (a) Example distribution of burnt (black) and unburnt (white) cells from one realisation of a wind-driven fire after line ignition at $x = 0$. A homogeneous fuel distribution having $\tau_{ign} = 10$ s and $\tau_{burn} = 360$ s is considered for this example. The wind speed is 25 m/s and modelling parameters are taken from Table 2. (b) Active fire particles coloured by their burning state under the same conditions. (c) Time evolution of the flame front position (calculated based on the 50% isoline of a burn progress factor that considers the burning state of all cells averaged over the direction of the ignition line and over 20 realisations) for different combinations of τ_{burn} and τ_{ign} and two strategies for HRR treatment: $Y_{init} = 1$ and $Y_{init} = f(t)$. (d) Schematic representation of the two implementation strategies for Y_{init}. Left: Release of particles with constant $Y_{init} = 1$. Right: release of particles with a triangular shape for $Y_{init}(t)$. (e) Propagation speed as a function of Δx and N_p for two HRR implementation strategies and different combinations of τ_{burn} and τ_{ign} (based on 20 realisations). (For interpretation of the references to colour in this figure legend, the reader is referred to the web version of this article.)

remote cells. Y_{lim} dictates the expiration of the particles, whereas the initial state Y_{init} emulates the magnitude of the HRR at the time of emission. In this work, it was assumed that Y_{init} is always constant and equal to unity, which in some cases may lead to an overestimation of the total energy release and therefore to a greater sensitivity of the model to numerical parameters, such as N_p and the size of the grid. A way to improve on the above is to replace the particle state generation and decay mechanisms with a more quantitative energy balance that could potentially include a series of volatilisation, oxidation, air entrainment, and heat transfer processes. Instead of a particle state (or normalised temperature difference), each cell and particle could be associated with a (measurable) amount of enthalpy or a bulk temperature, although more modelling parameters would be required to capture the underlying phenomena. Another strategy that does not involve as many parameters is to retain the model formulation of this work and to adjust the value of Y_{init} over time. For various fuel types and materials, the temporal profile $Y_{init}(t)$ could then be calibrated against experiments, satellite data, or more physics-based approaches, along with other flammability parameters.

In the following, we consider a simple example of a varying profile for $Y_{init} = f(t)$ and we evaluate the behaviour of the model in canonical problems of line ignition and wind-driven propagation in a domain with a homogeneous fuel distribution. A constant wind speed of 25 m/s, similar to the initial westerly wind in the Marshall fire, is considered, together with the modelling parameters of Table 2. Under these conditions, four fuel types are then investigated having combinations of τ_{ign}/τ_{burn}: (i) 10 s/360 s; (ii) 10 s/1800 s; (iii) 180 s/360 s and (iv) 180 s/1800 s. For the short τ_{ign} fuel types, that is, (i) and (ii), a convection-influenced non-firebranding flame should be established, whereas a firebranding mechanism should also be present for the longer τ_{ign} cases that are more relevant to the burning of wooden houses and buildings. An example distribution of burnt *vs.* unburnt cells from one realisation at a time after ignition is shown in Fig. A.1a for fuel type (i), while the active particles in the same instance are shown in Fig. A.1b. For these problems, two different implementations of the energy release are considered: a constant profile ($Y_{init} = 1$) and an evolving profile ($Y_{init} = f(t)$). For the latter, a triangular shape is selected with a maximum value of $Y_{st,p=1}$ at the start of particle release, but this profile is only of indicative value. However, it could still be realistic in some cases, for example, for some cellulosic fuels, where the HRR shows a distinct peak after an induction period and a quasi-linear decrease over time (e.g., see [42]). Fig. A.1d depicts a comparison of the two implementations for particles released uniformly throughout the burning duration of a cell.

For both implementations, the position of the flame front can be calculated based on the 50% isoline of a burn progress factor (BPF) that considers the burning state of all cells (0 for unburnt or 1 for ignited/burnt as in Fig. A.1a) averaged over the direction of the ignition line and over several realisations, similar to Ref. [19]. As shown in Fig. A.1c for a nominal grid size of $\Delta x = 5$ m, $N_p = 25$ particles per cell and a particle Courant number $c = 0.5$, the purely convection-influenced non-firebranding flames are characterised by a linear evolution of the flame front position, while the longer τ_{ign} fuels show a "start-stop" behaviour that results in a step-like evolution. Because τ_{ign} is large, e.g., as expected for a wooden house, there must be a time difference until propagation can occur from one cell to the next (seen here as a stagnant flame front position over equidistant durations), similar to what Himoto et al. [43] reported as the time difference of flashover from one model house to the adjacent. It is evident that this behaviour can be reproduced by an appropriate selection of the timescales controlling the release and decay of particles. It is also evident that the implementation of Y_{init} has no effect in short

τ_{ign} fuels (the associated curves overlap almost exactly), but results in slower propagation for longer τ_{ign} cases. This observation is important because it underscores that highly flammable fuels with short burning timescales can be largely insensitive to how the energy release is treated, while the opposite applies to slower-burning fuels. However, using suitable values for the burning timescales, the flame front position could always be matched between the two implementation options, which is a desirable feature of the model.

More importantly, we are interested in the (quasi-steady) propagation speed, here calculated based on the step locations for long τ_{ign} cases and by the final flame front position for short τ_{ign} cases. In particular, for short τ_{ign} cases, the propagation speed is $S_f \approx 3$ m/s. This value is representative of 1 to 10-h fuels (grasses and other plants) typically considered with the well-established Rothermel model [52], as described in Ref. [53] with minor modifications by Albini [54,55]. Firebrand-influenced flames cannot be considered with this model. Taking into account zero slope effects, nominal values for the characteristics of the fuel particles, a fuel array with a surface area-to-volume ratio of 3000 ft^{-1} (≈9842.5 m^{-1}) and a reasonably low moisture content of 2% (the dead fuel moisture of extinction is taken 15%), we obtain a propagation speed $S_f \approx 3.16$ m/s that agrees well with the highly flammable fuels investigated here. Evidently, different values for the surface area-to-volume ratio and moisture content could be applicable, for example, $S_f \approx 3.55$ m/s for 3% moisture and 3500 ft^{-1} (≈11483 m^{-1}), so a more accurate comparison with the Rothermel model requires a conversion of the fuel models and the environmental factors typically used to be appropriately converted into the flammability parameters of *FireSPIN*.

Furthermore, we are interested in the sensitivity of S_f to numerical parameters such as the grid size and the number of particles per cell. For this purpose, computations with different values for Δx and N_p are shown in Fig. A.1d. It is evident that when $Y_{init} = 1$, S_f can vary with both Δx and N_p, and in some cases substantially, as also observed in Section 5. Note, for example, the decrease in S_f with finer resolutions when the first three fuels are considered, that is, (i) to (iii). In contrast, for these cases, the propagation speed is not sensitive to numerical parameters when $Y_{init} = f(t)$, indicating a sufficient level of statistical convergence with a small or high particle density but also with a coarse or fine resolution. Some degree of sensitivity can only be observed for the slowly burning fuel (iv), indicating that a higher number of particles per cell should perhaps be used at coarser resolutions to better represent the energy release. In conclusion, the present framework allows several improvements to be introduced, thus resulting in a comprehensive WUI modelling capability.

Appendix B. Supplementary data

Supplementary material related to this article can be found online at https://doi.org/10.1016/j.firesaf.2023.103795.

References

[1] M.A. Finney, FARSITE: Fire Area Simulator-Model Development and Evaluation, Tech. rep., U.S. Department of Agriculture, Forest Service, Rocky Mountain Research Station, 1998, http://dx.doi.org/10.2737/rmrs-rp-4.

[2] A. Duane, M. Piqué, M. Castellnou, L. Brotons, Predictive modelling of fire occurrences from different fire spread patterns in Mediterranean landscapes, Int. J. Wildland Fire 24 (3) (2015) 407–418, http://dx.doi.org/10.1071/WF14040.

[3] A. Sullivan, J. Sharples, S. Matthews, M. Plucinski, A downslope fire spread correction factor based on landscape-scale fire behaviour, Environ. Model. Softw. 62 (2014) 153–163, http://dx.doi.org/10.1016/j.envsoft.2014.08.024.

[4] A. Duane, N. Aquilué, A. Gil-Tena, L. Brotons, Integrating fire spread patterns in fire modelling at landscape scale, Environ. Model. Softw. 86 (2016) 219–231, http://dx.doi.org/10.1016/j.envsoft.2016.10.001.

[5] P.L. Andrews, Current status and future needs of the BehavePlus Fire Modeling System, Int. J. Wildland Fire 23 (1) (2014) 21, http://dx.doi.org/10.1071/WF12167.

[6] C.W. Ott, B. Adhikari, S.P. Alexander, P. Hodza, C. Xu, T.A. Minckley, Predicting fire propagation across heterogeneous landscapes using WyoFire: A Monte Carlo-Driven Wildfire Model, Fire 3 (4) (2020) 71, http://dx.doi.org/10.3390/fire3040071.

[7] X. Li, H. Gao, M. Zhang, S. Zhang, Z. Gao, J. Liu, S. Sun, T. Hu, L. Sun, Prediction of forest fire spread rate using UAV images and an LSTM model considering the interaction between fire and wind, Remote Sens. 13 (21) (2021) 4325, http://dx.doi.org/10.3390/rs13214325.

[8] A.L. Sullivan, Wildland surface fire spread modelling, 1990 - 2007. 1: Physical and quasi-physical models, Int. J. Wildland Fire 18 (4) (2009) 349, http://dx.doi.org/10.1071/WF06143.

[9] A. Bakhshaii, E. Johnson, A review of a new generation of wildfire–atmosphere modeling, Can. J. Forest Res. 49 (6) (2019) 565–574, http://dx.doi.org/10.1139/cjfr-2018-0138.

[10] W. Jiang, F. Wang, L. Fang, X. Zheng, X. Qiao, Z. Li, Q. Meng, Modelling of wildland-urban interface fire spread with the heterogeneous cellular automata model, Environ. Model. Softw. 135 (2021) 104895, http://dx.doi.org/10.1016/j.envsoft.2020.104895.

[11] A. Trucchia, M. D'Andrea, F. Baghino, P. Fiorucci, L. Ferraris, PROPAGATOR: An operational cellular-automata based wildfire simulator, Fire 3 (3) (2020) 26, http://dx.doi.org/10.3390/fire3030026.

[12] S. Zhao, Simulation of mass fire-spread in urban densely built areas based on irregular coarse cellular automata, Fire Technol. 47 (3) (2011) 721–749, http://dx.doi.org/10.1007/s10694-010-0187-4.

[13] A. Alexandridis, L. Russo, D. Vakalis, G. Bafas, C. Siettos, Wildland fire spread modelling using cellular automata: evolution in large-scale spatially heterogeneous environments under fire suppression tactics, Int. J. Wildland Fire 20 (5) (2011) 633–647, http://dx.doi.org/10.1071/WF09119.

[14] M. de Gennaro, Y. Billaud, Y. Pizzo, S. Garivait, J.-C. Loraud, M. El Hajj, B. Porterie, Real-time wildland fire spread modeling using tabulated flame properties, Fire Saf. J. 91 (2017) 872–881, http://dx.doi.org/10.1016/j.firesaf.2017.03.006.

[15] A. Collin, D. Bernardin, O. Sero-Guillaume, A physical-based cellular automaton model for forest-fire propagation, Combust. Sci. Technol. 183 (4) (2011) 347–369, http://dx.doi.org/10.1080/00102202.2010.508476.

[16] Y. Liu, H. Liu, Y. Zhou, C. Sun, Spread vector induced cellular automata model for real-time crown fire behavior simulation, Environ. Model. Softw. 108 (2018) 14–39, http://dx.doi.org/10.1016/j.envsoft.2018.07.005.

[17] J. Adou, A. Brou, B. Porterie, Modeling wildland fire propagation using a semi-physical network model, Case Stud. Fire Saf. 4 (2015) 11–18, http://dx.doi.org/10.1016/j.csfs.2015.05.003.

[18] I. Karafyllidis, A. Thanailakis, A model for predicting forest fire spreading using cellular automata, Ecol. Model. 99 (1) (1997) 87–97, http://dx.doi.org/10.1016/S0304-3800(96)01942-4.

[19] E. Mastorakos, S. Gkantonas, G. Efstathiou, A. Giusti, A hybrid stochastic Lagrangian - cellular automata framework for modelling fire propagation in inhomogeneous terrains, Proc. Combust. Inst. 39 (2022) http://dx.doi.org/10.1016/j.proci.2022.07.240, (in press).

[20] B. Gabbert, Marshall fire updated damage assessment: 1,084 residences destroyed, Wildfire Today (2022) URL https://wildfiretoday.com/2022/01/07/marshall-fire-updated-damage-assessment-1084-residences-destroyed/.

[21] B. Gabbert, Wind-driven wildfire burns hundreds of homes near Boulder, Colorado, Wildfire Today (2022) URL https://wildfiretoday.com/2021/12/30/wind-driven-wildfire-burns-homes-near-boulder-colorado/.

[22] Boulder Office of Emergency Management, Boulder County Sheriff's Office, City of Louisville and Louisville Fire District and other partner agencies, Marshall Fire After-Action Report (AAR), 2022.

[23] Wikipedia, Marshall fire, 2022, URL https://en.wikipedia.org/wiki/Marshall_Fire.

[24] WikiMili, Marshall fire, 2022, URL https://wikimili.com/en/Marshall_Fire.

[25] National Weather Service Denver/Boulder CO, High winds and marshall fire on december 30th, 2021, URL https://www.weather.gov/bou/MarshallFire20211230.

[26] R.G. Fovell, M.J. Brewer, R.J. Garmong, The december 2021 Marshall fire: Predictability and gust forecasts from operational models, Atmosphere 13 (5) (2022) 765, http://dx.doi.org/10.3390/atmos13050765.

[27] A. Revkin, When wildfire comes to town – amid the Marshall fire's urban ashes, hints of a less combustible future, Sustain What (2022) URL https://revkin.bulletin.com/when-wildfire-comes-to-town-amid-the-marshall-fire-s-urban-ashes-hints-of-a-less-combustible-future.

[28] J. Brown, P. Jesse, The Minute-by-Minute Story of the Marshall Fire's Wind-Fueled Tear through Boulder County, The Guardian, 2022, URL https://coloradosun.com/2022/01/06/marshall-fire-boulder-county-timeline/.

[29] S.B. Pope, Lagrangian PDF methods for turbulent flows, Annu. Rev. Fluid Mech. 26 (1994) 23–63, http://dx.doi.org/10.1146/annurev.fl.26.010194.000323.

[30] C. Vassilicos, Dissipation in turbulent flows, Annu. Rev. Fluid Mech. 47 (1) (2015) 95–114, http://dx.doi.org/10.1146/annurev-fluid-010814-014637.

[31] M. Cruz, M. Alexandre, The 10% wind speed rule of thumb for estimating a wildfire's forward rate of spread in forests and shrublands, Ann. For. Sci. 76 (2) (2019) 1–11, http://dx.doi.org/10.1007/s13595-019-0829-8.

[32] R. Sun, S. Krueger, M. Jenkins, M. Zulauf, J. Charney, The importance of fire - atmosphere coupling and boundary-layer turbulence to wildfire spread, Int. J. Wildland Fire 18 (1) (2009) 50–60, http://dx.doi.org/10.1071/WF07072.

[33] W.E. Heilman, C.B. Clements, D. Seto, X. Bian, K.L. Clark, N.S. Skowronski, J.L. Hom, Observations of fire-induced turbulence regimes during low-intensity wildland fires in forested environments: implications for smoke dispersion, Atmos. Sci. Lett. 16 (4) (2015) 453–460, http://dx.doi.org/10.1002/asl.581.

[34] S. Manzello, S. Suzuki, M. Gollner, A. Fernandez-Pello, Role of firebrand combustion in large outdoor fire spread, Prog. Energy Combust. Sci. 76 (2020) 100801, http://dx.doi.org/10.1016/j.pecs.2019.100801.

[35] E. Koo, P. Pagni, D. Weise, J. Woycheese, Firebrands and spotting ignition in large-scale fires, Int. J. Wildland Fire 19 (7) (2010) 818–843, http://dx.doi.org/10.1071/WF07119.

[36] D. Haworth, Progress in probability density function methods for turbulent reacting flows, Prog. Energy Combust. Sci. 36 (2) (2010) 168–259, http://dx.doi.org/10.1016/j.pecs.2009.09.003.

[37] A. Neophytou, E. Richardson, E. Mastorakos, Spark ignition of turbulent recirculating non-premixed gas and spray flames: A model for predicting ignition probability, Combust. Flame 159 (4) (2012) 1503–1522, http://dx.doi.org/10.1016/j.combustflame.2011.12.015.

[38] J. Dewitz, National Land Cover Database (NLCD) 2016 Products (Ver. 2.0, July 2020), U.S. Geological Survey Data Release, 2019, http://dx.doi.org/10.5066/P96HHBIE.

[39] M.G. Cruz, J.S. Gould, S. Kidnie, R. Bessell, D. Nichols, A. Slijepcevic, Effects of curing on grassfires: II. Effect of grass senescence on the rate of fire spread, Int. J. Wildland Fire 24 (6) (2015) 838–848, http://dx.doi.org/10.1071/WF14146.

[40] M.G. Cruz, A. Sullivan, S. Kidnie, R. Hurley, D. Nichols, The Effect of Grass Curing and Fuel Structure on Fire Behaviour - Final Report, Tech. Rep. Client Report No. EP 166414, CSIRO Land and Water, Canberra, Australia, 2016, http://dx.doi.org/10.13140/RG.2.2.15444.91521.

[41] H.E. Anderson, Heat Transfer and Fire Spread, Tech. Rep. Res. Pap. INT-RP-69, U.S. Department of Agriculture, Forest Service, Intermountain Forest and Range Experiment Station, Ogden, Utah, 1969, p. 20.

[42] W.M. Pitts, Ignition of Cellulosic Fuels by Heated and Radiative Surfaces, Tech. Rep. NIST TN 1481, National Institute of Standards and Technology, Gaithersburg, MD, 2007, http://dx.doi.org/10.6028/nist.tn.1481.

[43] K. Himoto, M. Shinohara, A. Sekizawa, K. Takanashi, H. Saiki, A field experiment on fire spread within a group of model houses, Fire Saf. J. 96 (2018) 105–114, http://dx.doi.org/10.1016/j.firesaf.2018.01.003.

[44] T.N. Nandi, D. Yeo, Estimation of integral length scales across the neutral atmospheric boundary layer depth: A Large Eddy Simulation study, J. Wind Eng. Ind. Aerodyn. 218 (2021) 104715, http://dx.doi.org/10.1016/j.jweia.2021.104715.

[45] J.D. Holmes, Wind Loading of Structures, second ed., CRC Press, London, 2007, http://dx.doi.org/10.4324/9780203964286.

[46] WeatherForYou.com LLC, Weather Archives for Marshall Lake, CO, 2022, URL https://www.weatherforyou.com/reports/index.php?forecast=pass&pass=archivenws&zipcode=&pands=&place=marshall+lake&state=co&icao=&country=us&month=12&day=30&year=2021&dosubmit=Go.

[47] WeatherForYou.com LLC, Weather Archives for Louisville, CO, 2022, URL https://www.weatherforyou.com/reports/index.php?forecast=pass&pass=archivenws&zipcode=80027&pands=&place=louisville&state=co&icao=&country=us&month=12&day=30&year=2021&dosubmit=Go.

[48] D. Boychuk, W.J. Braun, R.J. Kulperger, Z.L. Krougly, D.A. Stanford, A stochastic model for forest fire growth, INFOR: Inf. Syst. Oper. Res. 45 (1) (2007) 9–16, http://dx.doi.org/10.3138/infor.45.1.9.

[49] D. Boychuk, W.J. Braun, R.J. Kulperger, Z.L. Krougly, D.A. Stanford, A stochastic forest fire growth model, Environ. Ecol. Stat. 16 (2) (2009) 133–151, http://dx.doi.org/10.1007/s10651-007-0079-z.

[50] H.H. Richardson, Photos: Marshall Fire Aerial Images Show Scale of Devastation, The Denver Post, 2022, URL https://www.denverpost.com/2022/01/02/marshall-fire-aerial-photos/.

[51] R.E. Burgan, R.C. Rothermel, BEHAVE: Fire Behavior Prediction and Fuel Modeling System–FUEL Subsystem, Tech. Rep. General Technical Report INT-167, U. S. Department of Agriculture, Forest Service, Intermountain Forest and Range Experiment Station, Ogden, UT, 1984, http://dx.doi.org/10.2737/INT-GTR-167.

[52] R.C. Rothermel, A Mathematical Model for Predicting Fire Spread in Wildland Fuels, Tech. Rep. Research paper No. INT-115, U. S. Department of Agriculture, Forest Service, Intermountain Forest and Range Experiment Station, Ogden, UT, 1972.

[53] P.L. Andrews, The Rothermel Surface Fire Spread Model and Associated Developments: A Comprehensive Explanation, Tech. Rep. General Technical Report RMRS-GTR-371, U.S. Department of Agriculture, Forest Service, Rocky Mountain Research Station, Ft. Collins, CO, 2018, http://dx.doi.org/10.2737/RMRS-GTR-371.

[54] F.A. Albini, Computer-Based Models of Wildland Fire Behavior: A User's Manual, Tech. rep., U. S. Department of Agriculture, Forest Service, Intermountain Forest and Range Experiment Station, Ogden, UT, 1976.

[55] F.A. Albini, Estimating Wildfire Behavior and Effects, Tech. Rep. General Technical Report INT-30, U. S. Department of Agriculture, Forest Service, Intermountain Forest and Range Experiment Station, Ogden, UT, 1976.